

ATCA 1.2 cm Observations of the Massive Star Forming Region G305.2+0.2

Andrew J. Walsh^{1,2*}, Jacqueline F. Chapman³,
Michael G. Burton¹, Mark Wardle³ and T. J. Millar⁴

¹*School of Physics, University of New South Wales, Sydney, NSW 2052, Australia*

²*School of Maths, Physics and IT, James Cook University, 4814, Australia*

³*Department of Physics, Macquarie University, Sydney, NSW 2109, Australia*

⁴*Astrophysics Research Centre, School of Mathematics and Physics, Queen's University Belfast, Belfast BT7 1NN, UK*

18 November 2018

ABSTRACT

We report on Australia Telescope observations of the massive star forming region G305.2+0.2 at 1.2 cm. We detected emission in five molecules towards G305A, confirming its hot core nature. We determined a rotational temperature of 26 K for methanol. A non-LTE excitation calculation suggests a kinematic temperature of order 200 K. A time dependent chemical model is also used to model the gas phase chemistry of the hot core associated with G305A. A comparison with the observations suggest an age of between 2×10^4 and 1.5×10^5 years. We also report on a feature to the SE of G305A which may show weak Class I methanol maser emission in the line at 24.933 GHz. The more evolved source G305B does not show emission in any of the line tracers, but strong Class I methanol maser emission at 24.933 GHz is found $3''$ to the east. Radio continuum emission at 18.496 GHz is detected towards two HII regions. The implications of the non-detection of radio continuum emission toward G305A and G305B are also discussed.

Key words: masers – stars: formation – infrared: ISM – ISM: molecules

1 INTRODUCTION

The study of the early stages of massive star formation (MSF) in our Galaxy has, until recently, received relatively little attention compared to low mass star formation. However, with the advent of telescopes, particularly in the millimetre (mm) and sub-mm part of the electromagnetic spectrum, it has become possible to study the earliest stages of MSF. This is the strongest part of their spectral energy distribution (SED) measurable from the ground. It also contains a myriad of complex molecular transitions, allowing investigation of the physics and chemistry surrounding these young sources.

G305.2+0.2 is a site of MSF in the southern Galactic plane. Class II methanol masers were reported in two positions by Norris et al. (1993): G305.21+0.21 (G305A) and G305.20+0.21 (G305B), separated by approximately $22''$. Walsh et al. (1999) observed this region in the near-infrared and found that whilst G305A is not associated with any infrared source, G305B is coincident with a bright and very reddened infrared source. More sensitive near-infrared observations by De Buizer (2003) indicate that there is indeed

a weak infrared source coincident with G305A, however, it is not clear if it is associated with the maser site or is instead an unrelated foreground star. Observations in the mid-infrared (10.5 and $20 \mu\text{m}$) by Walsh et al. (2001) confirm the infrared source associated with G305B has a steeply rising spectral energy distribution towards longer wavelengths. However, no mid-infrared source was found associated with G305A. The Galactic Legacy Infrared Mid-Plane Survey Extraordinaire (GLIMPSE) is a legacy science program of the *Spitzer Space Telescope*. It confirms the detection of a weak infrared source at the position of G305A at 3.6 and $4.5 \mu\text{m}$. However, the region shows much extended emission (see Figures 1a and 3b), which makes photometry unreliable.

Hill et al. (2005) have detected a strong 1.2 mm continuum source whose peak coincides with G305A (see figure 1 of Walsh & Burton (2006)). The 1.2 mm map also shows some extended emission in the direction of G305B, but the extended emission was poorly resolved. Because G305B appears to dominate the luminosity at shorter wavelengths (up to about $20 \mu\text{m}$) and G305A appears to dominate at longer wavelengths (1.2 mm), there will be a transition point at far-infrared wavelengths where the two sources will have equal brightnesses. Thus, it is impossible to tell which source is the most luminous, based on infrared data alone. Neither maser

* E-mail: andrew.walsh@jcu.edu.au

site is coincident with any detected radio continuum source (Phillips et al. 1998a). However, one might be expected from G305B, since extrapolation of its SED (Walsh et al. 2001) indicates it is powered by a star bright enough to produce an observable ultracompact (UC) HII region. Furthermore, it is not known why the brightest maser site, G305A is not associated with a bright infrared source, nor a radio continuum source and yet appears to be a strong source of continuum emission at 1.2 mm.

Walsh & Burton (2006) found G305A to be the local peak of emission for 1–0 transitions of ^{13}CO , HCO^+ and N_2H^+ , as well as transitions of CH_3CN and CH_3OH . NH_3 (1,1), (2,2) and (4,4) emission has been detected coincident with G305A (Steven Longmore, private communication 2007). This suggests G305A is a hot core and may be the most massive component in the region. The line and dust continuum emission appear to be slightly elongated in the direction of G305B. Therefore it appears G305B may be associated with a secondary hot core, which was spatially unresolved with the previous observations. Walsh & Burton (2006) also identified the possible prestellar massive core G305SW, which was only detected in N_2H^+ and shows narrow lines, compared to the emission elsewhere in the field of view. In this paper we attempt to better understand the nature of these sources by investigating both molecular line and continuum emission at 1.2 cm.

2 OBSERVATIONS

Observations towards G305.2+0.2 were carried out using two configurations of the ATCA in 2005. The first observations took place on 2005, May, 3-4th and utilised the 750A configuration. The second observations took place on 2005, September, 4th and utilised the H214 configuration. Details of each observing session are given below.

2.1 2005, May observations

Using the 750A configuration, we observed G305 with baselines ranging from 77 to 735 m, with five antennas, and baselines up to 3750 m when including antenna 6. However, data from antenna 6 were only used when observing masers. The primary beam for these observations was between $2.0'$ and $2.6'$, and the synthesised beam was between $3.2''$ and $4.9''$, when only 5 antennas were used. Observations were made towards a single position, with pointing centre $13^{\text{h}} 11^{\text{m}} 10.6^{\text{s}}$, right ascension and $-62^\circ 34' 38''$ declination (J2000). We spent a total of 12 hours observing G305 in this configuration, which included time for primary calibration on 1934-638, bandpass calibration on 1253-055 and phase calibration on 1414-59. We observed in a frequency-switching mode, with main (spectral line) frequencies being 18199 MHz and 24932 MHz, which include emission lines of cyanoacetylene (HC_3N (2–1)) and the K=2 ladder of methanol (CH_3OH), respectively. Assumed rest frequencies for these lines are given in Table 1. Each frequency was observed with 256 channels over a bandwidth of 16 MHz, resulting in a velocity resolution of 1.0 km s^{-1} and 0.75 km s^{-1} per channel at the HC_3N and CH_3OH line frequencies, respectively. In addition to the spectral lines, continuum emission was observed at 18496 MHz with a bandwidth of 128 MHz.

2.2 2005, September observations

Using the H214C hybrid configuration, we observed G305 with baselines ranging from 82 m to 240 m with five antennas. The primary beam for these observations was between $2.0'$ and $2.6'$, and the synthesised beam was between $8.6''$ and $11.8''$. Observations were made with a single point, with pointing centre $13^{\text{h}} 11^{\text{m}} 6.25^{\text{s}}$, right ascension and $-62^\circ 34' 53''$ declination (J2000). The reason for the different pointing centre to the 2005, May observations was to cover the newly discovered source G305SW (Walsh & Burton 2006). We spent a total of 11 hours observing G305 in this configuration, which included time for primary calibration on 1934-638, bandpass calibration on 0537-441 and phase calibration on 1414-59. We observed in a frequency-switching mode, with five pairs of spectral line frequencies, the details of which are given in Table 1.

Observations made in this session have poorer spatial and spectral resolution than the 2005, May session. The main implication of this is that the spectral resolution is insufficient to identify most systemic motions, although we are able to identify detections and discriminate between emission from G305A and G305B.

3 RESULTS

Approximately half the lines that were searched were detected, and details of these lines are given in Table 2. The table also includes details of those lines that were not detected, together with their upper limits. Since the 2005 September observing run was conducted using a relatively poor spatial and spectral resolution, we do not know line widths or precise locations for most of the lines detected during this time. In the last column of Table 2, we list the position of the emission and nearest association if it is not found coincident with G305A or G305B. The observations of methanol and cyanoacetylene conducted in 2005 May have both higher spatial and spectral resolution, and so we report more detailed results on each below.

3.1 CH_3OH (methanol)

The bandpass covered three lines of methanol during these observations, as listed in Table 1. We find strong, narrow line emission from the J=4 line close to the position of G305B, but not coincident (Figure 1). The emission appears to be offset from G305B by approximately $3''$ to the east ($13 11 10.89 -62 34 38.5$ J2000). In addition to this, weaker emission is seen in all three methanol lines at the position of G305A (Figure 1). The methanol emission around G305A also shows extended emission to the south-south-east, extending by approximately $5''$. This extension, which we refer to as G305A(SE), is strongest in the J=4 methanol line, but the other two lines are also detected here. We note also that the J=4 methanol line appears to be very narrow at this position. So the relative methanol line intensities and line width are reminiscent of a weaker version of the emission seen close to G305B.

Table 1. Properties of observed lines. The notation for each line in the second column either conforms to the structure of ($J_{\text{upper}} - J_{\text{lower}}$) or ($J_{-K,+K} - J_{-K,+K}$).

Date	Observed Line	Rest Frequency (MHz)	Primary Beam (')	Synthesized Beam (")	Bandwidth (MHz)	Velocity Resolution (km s^{-1})
2005 MAY 3-4	HC ₃ N (2-1)	18196.226	2.6	4.9	16	1.0
2005 MAY 3-4	CH ₃ OH (3 _{2,1} - 3 _{1,2}) E	24928.700	2.0	3.2	16	0.75
	CH ₃ OH (4 _{2,2} - 4 _{1,3}) E	24933.470				
	CH ₃ OH (2 _{2,0} - 2 _{1,1}) E	24934.380				
2005 SEP 4	NH ₃ (1,1)	23694.496	2.0	9.0	32	3.2
	NH ₃ (2,2)	23722.633	2.0	9.0	32	3.2
2005 SEP 4	H ₂ O (6 _{1,6} - 5 _{2,3})	22235.080	2.1	9.6	32	3.4
	CH ₃ OCHO (2 _{1,2} - 1 _{1,1}) E	22827.741	2.1	9.4	32	3.3
	CH ₃ OCHO (2 _{1,2} - 1 _{1,1}) A	22828.134	2.1	9.4	32	3.3
	NH ₃ (3,2)	22834.185	2.1	9.4	32	3.3
2005 SEP 4	CH ₃ OH (8 _{2,6} - 8 _{1,7}) E	25294.417	1.9	8.6	64	11.9
	DC ₃ N (3-2)	25329.437	1.9	8.5	64	12.0
2005 SEP 4	OCS (2-1)	24325.927	2.0	8.8	64	12.3
2005 SEP 4	CH ₃ CN (1-0)	18399.892	2.6	11.6	32	4.1
2005 SEP 4	DC ₃ N (2-1)	16886.310	2.8	12.7	64	17.8
	H91 β (RRL)	16894.200	2.8	12.7	64	17.8
	HC ₇ N (15-14)	16919.979	2.8	12.7	64	17.7
	HC ₅ N (7-6)	18638.616	2.6	11.5	32	4.0

3.2 HC₃N (cyanoacetylene)

We only detect cyanoacetylene coincident with the position of G305A (Figure 2). The emission appears to be unresolved spatially, but is resolved spectrally with a line width of 5.1 km s^{-1} . Cyanoacetylene can be formed by neutral-neutral reactions in interstellar space (Fukuzawa & Osamura 1997), and so is likely a precursor molecule that is present at the onset of star formation. Millar et al. (1997) indicate that cyanoacetylene can also be formed in hot cores. Their models also suggest that the cyanoacetylene abundance is greatly reduced after about 10^5 years. Implications of the time-dependant chemistry are discussed further in §5.

3.3 Continuum emission

Our 2005 May data included a frequency (18496 MHz) devoted to continuum emission, with a bandwidth of 128 MHz. The continuum map is shown in Figure 3. Two prominent continuum features appear in the map: the compact HII region G305HII (Walsh & Burton 2006), and a similarly sized compact HII region about $30''$ to the SE of G305A, which we call G305HII(SE). We assume that each HII region has its own powering source that is unrelated to either G305A or G305B. This is because there is a large separation between the HII regions and G305A or G305B. Also, the powering source for G305HII appears as a near-infrared source at the centre of the radio continuum con-

tours (Walsh & Burton 2006). The integrated intensity of the emission from G305HII is 174 mJy and the integrated intensity of the emission from G305HII(SE) is 57 mJy. Line-free channels from the 2005 September data can be used to reconstruct the fluxes of the HII regions between 16 and 25 GHz. A plot of the distribution of fluxes with frequency is shown in Figure 4. Overall, it appears that the flux remains constant over the frequency range, which is consistent with optically thin free-free emission. There are apparent changes in flux in both sources which are matched in frequency. This is most likely due to errors in the absolute flux calibration, which precludes us from assessing small changes in the slope of the continuum emission. Phillips et al. (1998a) have previously measured the continuum flux of G305HII at 8.6 GHz to be 195 mJy, which is also consistent with optically thin free-free emission.

We can make an estimate of the type of stars that give rise to these HII regions, using equation (4) of Kurtz, Churchwell & Wood (1994). Here, we assume the distance to G305 is 3.9 kpc, the electron temperature (T_e) is 10000 K and $a(\nu, T_e) = 1$. If we also assume that no photons are absorbed by dust within the HII regions, then we find the rate of emission of Lyman continuum photons to be $2.7 \times 10^{47} \text{ s}^{-1}$ and $8.8 \times 10^{46} \text{ s}^{-1}$ for G305HII and G305HII(SE), respectively. Using the tables of Panagia (1973), these rates are equivalent to slightly earlier than a B0 spectral type for G305HII and slightly later than a B0 spectral type for G305HII(SE). If, however, 90% of the Lyman photons are absorbed by dust within the HII regions,

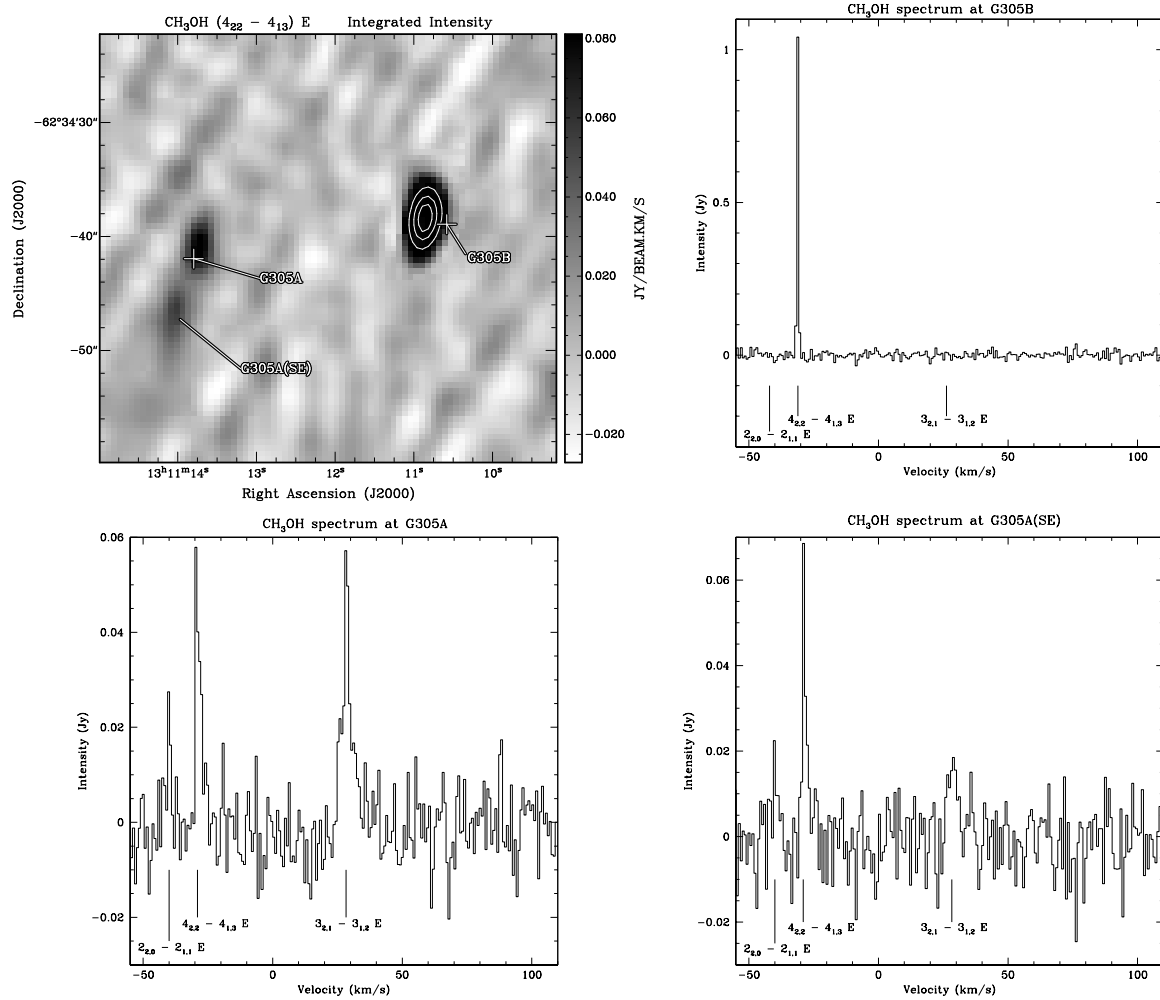


Figure 1. (a) CH₃OH integrated intensity map of the J=4 line. Plus symbols show the positions of the 6.7 GHz CH₃OH maser sites G305A and G305B. Contour levels are 0.2, 0.4 and 0.6 Jy/beam.km/s. (b) CH₃OH spectrum towards the bright line 3'' to the east of G305B, at 13 11 10.89 -62 34 38.5 (J2000). (c) CH₃OH spectrum towards G305A. (d) CH₃OH spectrum towards G305A(SE), at 13 11 14.00 -62 34 46.5 (J2000).

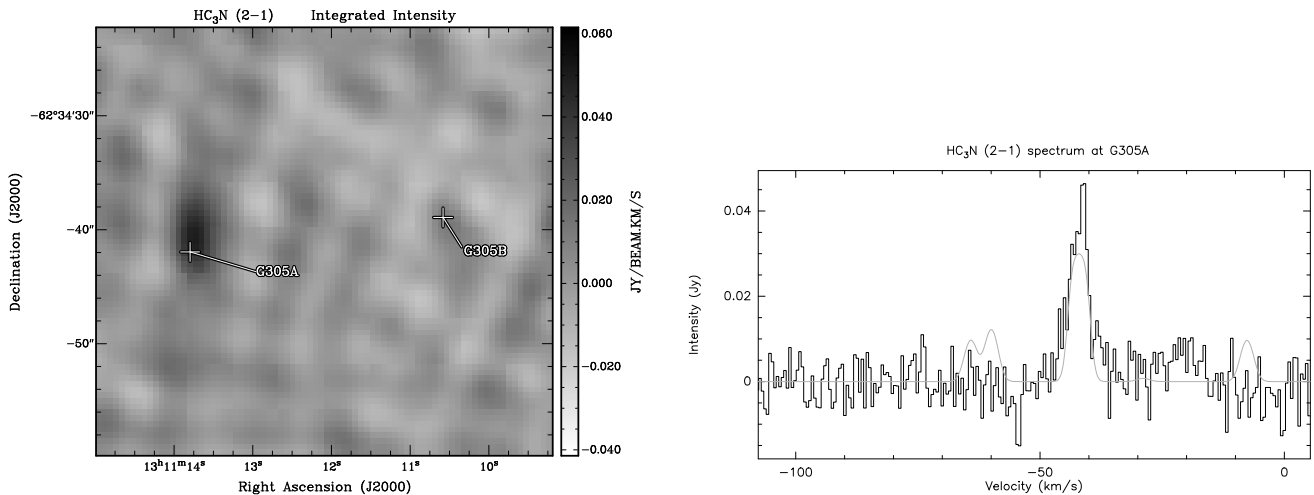


Figure 2. (a) HC₃N integrated intensity map. Plus symbols show the positions of the maser sites G305A and G305B. (b) HC₃N spectrum towards G305A. The dotted line is a best fit model to the HC₃N hyperfine structure, holding the optical depth constant at 0.1. Because we do not see any signs of the hyperfine components, we will assume the emission is optically thin.

Table 2. Properties of detections and non-detections. The notation for each line either conforms to the structure of ($J_{\text{upper}} - J_{\text{lower}}$) or ($J_{-K,+K} - J_{-K,+K}$). Only detections for each transition are reported, except where no detection anywhere was made. In the case of a non-detection, then 1σ upper limit for the integrated intensity is given. The last column lists names that are used in the text as a reference for the position of the emission.

Observed Line	Position (J2000)	Integrated Intensity (K.km s^{-1})	Peak Velocity (km s^{-1})	Line Width (km s^{-1})	Association
HC ₃ N (2-1)	13 11 13.71 -62 34 40.5	9.6	-41.9	5.1	G305A
CH ₃ OH (3 _{2,1} - 3 _{1,2}) E	13 11 13.71 -62 34 41.0	12.2	-39.8	5.1	G305A
CH ₃ OH (4 _{2,2} - 4 _{1,3}) E	13 11 13.71 -62 34 41.0	11.8	-39.8	4.8	G305A
CH ₃ OH (2 _{2,0} - 2 _{1,1}) E	13 11 13.71 -62 34 41.0	9.0	-40.0	5.9	G305A
CH ₃ OH (3 _{2,1} - 3 _{1,2}) E	13 11 14.00 -62 34 46.5	4.0	-39.7	2.5	G305A(SE)
CH ₃ OH (4 _{2,2} - 4 _{1,3}) E	13 11 14.00 -62 34 46.5	5.3	-39.7	2.1	G305A(SE)
CH ₃ OH (2 _{2,0} - 2 _{1,1}) E	13 11 14.00 -62 34 46.5	2.3	-39.8	2.9	G305A(SE)
CH ₃ OH (3 _{2,1} - 3 _{1,2}) E	-	<1.2	-	-	-
CH ₃ OH (4 _{2,2} - 4 _{1,3}) E	13 11 10.89 -62 34 39.0	46	-42.1	<0.75	3'' E of G305B
CH ₃ OH (2 _{2,0} - 2 _{1,1}) E	-	<1.2	-	-	-
NH ₃ (1,1)	13 11 13.71 -62 34 41.0	84	-	-	G305A
NH ₃ (2,2)	13 11 13.71 -62 34 41.0	11	-	-	G305A
OCS (2-1)	13 11 14.08 -62 34 39.0	3.9	-42	<12	G305A
NH ₃ (3,2)	13 11 13.71 -62 34 41.0	15.0	-39	<13	G305A
H ₂ O (6 _{1,6} - 5 _{2,3})	13 11 13.71 -62 34 41.0	18000	-40	<3.4	G305A
H ₂ O (6 _{1,6} - 5 _{2,3})	13 11 13.50 -62 34 31.0	25	-52	<3.4	10'' N of G305A
H ₂ O (6 _{1,6} - 5 _{2,3})	13 11 08.29 -62 34 45.0	6.3	+4	<3.4	14'' SW of G305B
CH ₃ OCHO (2 _{1,2} -1 _{1,1}) E	-	<0.11	-	-	-
CH ₃ OCHO (2 _{1,2} -1 _{1,1}) A	-	<0.11	-	-	-
CH ₃ OH (8 _{2,6} - 8 _{1,7}) E	13 11 10.89 -62 34 39.0	130	-43	<12	3'' E of G305B
DC ₃ N (3-2)	-	<0.03	-	-	-
CH ₃ CN (1-0)	-	<0.05	-	-	-
DC ₃ N (2-1)	-	<0.03	-	-	-
H91 β (RRL)	13 11 08.87 -62 34 41.0	3.7	-43	<18	G305HII
HC ₇ N (15-14)	-	<0.03	-	-	-
HC ₅ N (7-6)	-	<0.11	-	-	-

then these spectral types will be revised to O8 for G305HII and O9.5 for G305HII(SE). Note that we use the value of 90% absorption to illustrate how this affects the spectral type. We do not consider 90% as the most likely figure dust over, say 10% or 99%.

We do not see any continuum emission associated with either of the methanol maser sites G305A or G305B, with a 3σ detection limit of 0.15 mJy and 0.09 mJy, respectively. This is surprising as both sites are expected to harbour massive stars, which should have detectable radio continuum emission, as is the case for G305HII and G305HII(SE). G305A in particular appears to be the concentration for strong millimetre line emission (Walsh et al. 2006, and this work). This leads us to the conclusion that G305A at least, and probably G305B, are at a very early stage of evolution where any HII region has not had enough time to form and/or expand to an observable size and strength.

4 DISCUSSION

4.1 Maser emission in G305.2+0.2

As well as the two Class II 6.7 GHz methanol maser sites G305A and G305B, a number of emission features detected in this work may also be masers. Water masers are detected at three positions in the field: coincident with G305A, ap-

proximately 10'' N of G305A and approximately 14'' SW of G305B. This last maser site is coincident with the extended radio continuum emission of G305HII (Figure 3). The three water maser features appear over a velocity range of about 56 km s^{-1} (Figure 5). It is therefore likely that at least one of these features arises in an outflow, as water masers are commonly found in outflows (eg. Moscadelli, Cesaroni & Rioja (2005)), which can give rise to such high velocities.

The J=4 and J=8 methanol features exhibit very bright and narrow emission about 3'' to the east of G305B, where the Class II 6.7 GHz methanol maser lies. We suspect that both are Class I methanol masers (Müller, Menten & Mäder 2004). It is surprising that we see Class I and II methanol masers in close proximity to each other as it is unlikely that both Class I and II masers can be strong in the same place (Voronkov et al. 2005). However, we note that the 3'' projected offset between the two corresponds to 12000 AU (assuming a distance of 3.9 kpc), which is certainly well separated enough that there may be different physical conditions at the positions of the Class I and II masers. Figure 1 shows that G305A(SE) is a narrow line emission feature in the J=4 methanol line, which may also be a maser. Due to its intrinsic weakness, we cannot rule out the possibility that it is not a maser, but unusually narrow-lined thermal emission. We explore the possibility that this is thermal emission in the next subsection.

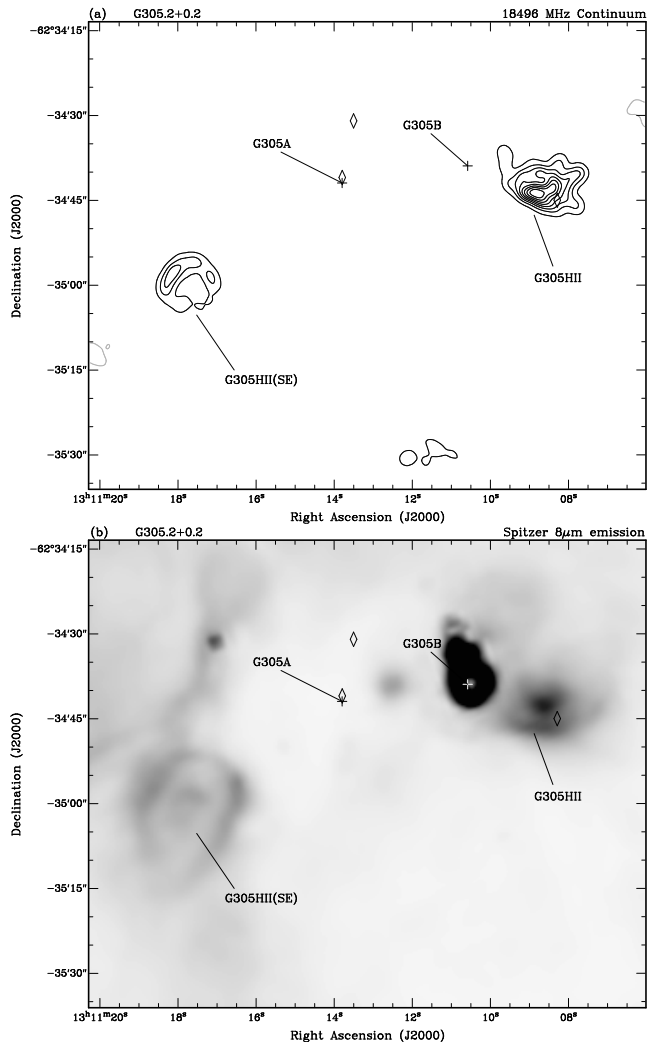


Figure 3. (a) 18496 MHz continuum emission towards G305. The two 6.67 GHz methanol maser sites G305A and G305B are indicated with the plus symbols. Water masers are indicated with diamond symbols. The contours are at 10, 20, ... 90% of the peak flux density, which is 22 mJy/beam. (b) Spitzer 8μm image towards G305. Very strong emission is seen coincident with G305B. This creates an artifact that extends to the NE of G305B. No emission is seen coincident with G305A.

4.2 Thermal CH₃OH (methanol)

For G305A, integrated intensities of the three thermal methanol lines are listed in Table 2. Assuming the lines are optically thin, we can estimate the methanol column density and rotation temperature using a rotation diagram analysis (Linke, Frerking & Thaddeus 1979), shown in Figure 6. We find a column density of $(9.6 \pm 4) \times 10^{15} \text{ cm}^{-2}$ and temperature of 26 K. The errorbars shown in Figure 6 are determined by the relative uncertainty in the line integrated intensities. This uncertainty derives from the fit performed to each line, as well as the inherent uncertainty in the image reconstruction process. However, it does not include an absolute calibration error. We estimate that the error in our flux determinations is approximately a factor of two, based on the flux calibration of the telescope. The size of this error is confirmed by comparing observations of the J=3 and 4 tran-

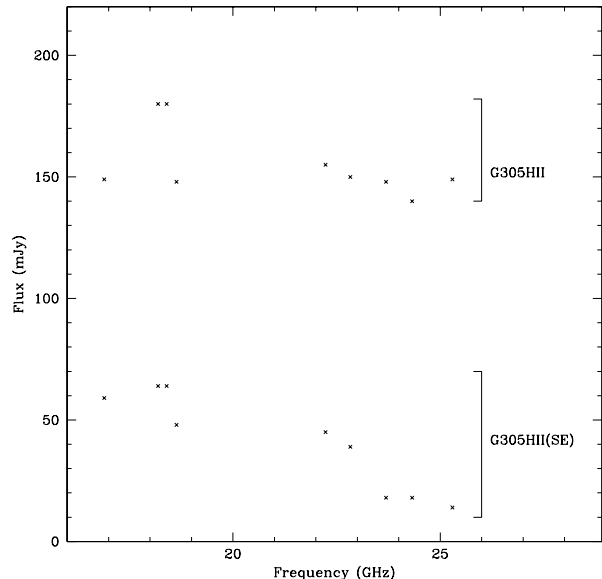


Figure 4. Continuum flux as a function of frequency for G305HII and G305HII(SE). The general trend is a flat distribution, consistent with optically thin free-free emission. The scatter seen in the points is likely due to the errors in the absolute flux calibration for each frequency and is therefore a good representation of the error in the flux of each HII region.

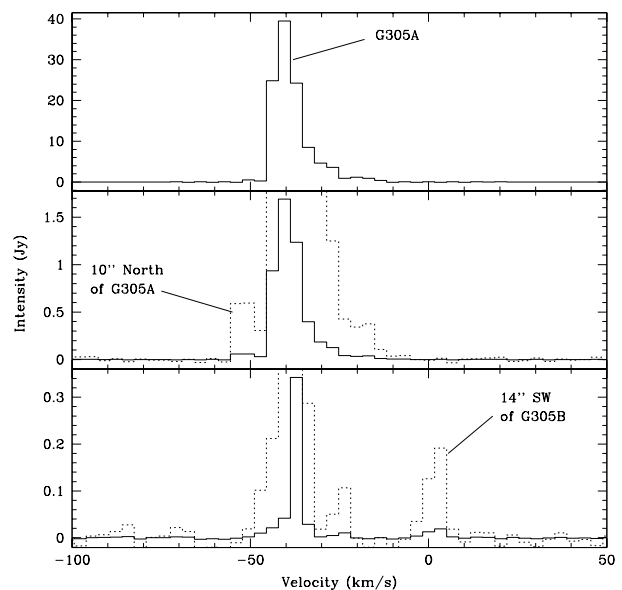


Figure 5. Water maser spectra for the three detected features. The strongest feature is shown in the top spectrum and is coincident with G305A. This feature also dominates the emission seen in the other spectra. The dotted lines in the middle and bottom spectra show a 10-fold increase in the intensity axis, to highlight the two weaker maser features that appear 10'' to the north of G305A (middle) and 14'' to the SW of G305B (bottom).

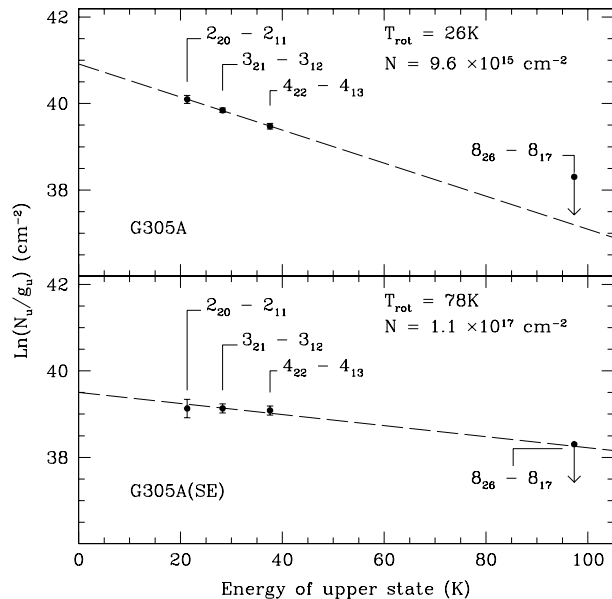


Figure 6. Methanol rotation diagram for G305A (top) and G305A(SE) (bottom). For each source, a straight (dashed) line is fitted through the three lower temperature transitions ($J=2,3$ and 4). The fitted rotational temperature and column density is given for each line. Whilst the $J=8$ upper limit is consistent with the fitted line for G305A, it is not possible to fit a line that is consistent with the $J=8$ upper limit for G305A(SE). The dotted line in the lower plot shows a fit through the $J=8$ line, which results in a column density of $1.1 \times 10^{17} \text{ cm}^{-2}$ and rotational temperature of 78 K.

sitions of methanol performed during both sessions in May and September. In addition to the three detected methanol lines, we also observed the $8_{26} - 8_{17}$ transition of methanol, but failed to detect it. Therefore, we include the upper limit for this transition in Figure 6. We find that the upper limit is consistent the best fit line to the other three points. Because the emission comes from regions which appear unresolved, we do not consider missing flux due to missing short UV spacings a significant problem.

For G305A(SE), we also fit the three methanol lines in Figure 6, as well as the non-detection in the $J=8$ line. Here we find a column density of $1.1 \times 10^{17} \text{ cm}^{-2}$ and a temperature of 78 K. The derived excitation temperature from the rotation diagram analysis does not have a physical interpretation as a kinetic temperature unless the gas density is above critical. Hence we perform, in §4.8, a non-LTE analysis to derive column densities and relative abundances. As mentioned in §4.1, the narrow linewidths of the detected methanol transitions at this position are suggestive of maser emission. In addition to this, the methanol spectrum at G305A(SE) is similar to the methanol maser spectrum $3''$ to the east of G305B – the $J=4$ feature is the strongest. Such maser emission could explain the unusual results of the rotational diagram analysis for G305(SE) and so we favour the explanation that this is weak maser emission.

4.3 HC₃N (Cyanoacetylene)

Cyanoacetylene possesses hyperfine structure in its ($2-1$) transition. However, no hyperfine components were observed, apart from the main two transitions at 18196.279 MHz. Figure 2 shows a fit to the data, assuming a total optical depth of 0.1. The satellite components do not appear above the modelled spectrum. Therefore, we can be confident the main line cyanoacetylene emission has an optical depth less than 0.1 (ie. optically thin).

Given the integrated intensity listed in Figure 2, and assuming an excitation temperature of 26 K from the methanol measurements, we calculate the cyanoacetylene column density is $4.0 \times 10^{14} \text{ cm}^{-2}$.

4.4 NH₃ (Ammonia)

Ammonia is detected towards G305A as an unresolved source. Because our low spectral resolution data cannot resolve the hyperfine structure of the ($1,1$) and ($2,2$) inversion transitions, we are unable to use our data to investigate the optical depth of the ammonia emission. However, higher spectral and spatial resolution ammonia observations (Steven Longmore, private communication 2007) detect ($1,1$), ($2,2$) and ($4,4$) emission coincident with G305A. The ($1,1$) and ($2,2$) transitions appear optically thick, so it is not possible to derive a reliable ammonia column density. The presence of ($4,4$) emission, which has an upper energy level of 200 K above ground, strongly suggests a hot component to G305A.

4.5 OCS (Carbonyl sulfide)

Carbonyl sulfide is detected as an unresolved source towards G305A. Assuming an excitation temperature of 26 K, we calculate a column density of $2.5 \times 10^{15} \text{ cm}^{-2}$ for this molecule.

4.6 H91 β radio recombination line

This radio recombination line is detected in the field and appears coincident with the HII region G305HII.

4.7 G305SW - a possible prestellar massive core

Walsh & Burton (2006) reported the detection of G305SW in N_2H^+ , but found it lacking in detectable emission in other tracers. They suggested this may be the signature of an extremely young and cold core, potentially prestellar. Unfortunately, G305SW lies just outside the primary beam of our 2005 May observations, but lies within the primary beam for the 2005 September observations. We found no evidence for emission in any of the tracers from the 2005 September observations. This is not surprising for most of the more complex molecules, but it is surprising that we did not detect any ammonia associated with G305SW. Since N_2H^+ and ammonia are chemically very similar, we would expect them to trace similar regions.

4.8 Derivation of column densities

The column densities listed above were derived with the assumption that the gas is in local thermodynamic equilibrium (LTE). The rotation diagram method used (see for example Figure 5) produces inaccurate temperatures and column densities if only limited line data is available (<3 lines). Moreover, the assumption of LTE is only valid for large densities. We present below, column densities derived from a non-LTE analysis of the molecular lines observed in Table 2.

Observations have shown CH₃OH accounts for a significant fraction of ice mantles relative to H₂O (Tielens & Allamandola 1987). It is believed that CH₃OH is formed on the surfaces of grains by the hydrogenation of CO on the grain surface (Charnley et al. 1992). Above temperatures of $\sim 90 - 100$ K, all ice species, including CH₃OH will be sublimated from the surfaces of grains. The abundance of CH₃OH should therefore increase in the inner warmer regions of hot cores. In §4.2, three CH₃OH lines were analyzed with a rotation diagram and a kinetic temperature of 26 K was derived. However, to release the methanol from the surfaces of grains, the temperature must have been of the order 90 – 100 K at some earlier time. It seems unlikely that the gas would have rapidly cooled to 26 K, and we attribute the low 26 K temperature to the inaccurate assumption of LTE.

In order to account for the discrepancy in the derived low (26 K) temperature using the rotation diagram analysis of the CH₃OH lines, we present below the results from a non-LTE radiative transfer model. A new analysis of the molecular lines in Table 2 produces new column density values and temperatures, which agree better with our understanding of the underlying physics and chemistry (see also §5). For this calculation, molecular data from Schöier et al. (2005) is used which includes energy levels, statistical weights, transition frequencies as well as collisional rate coefficients (for collisions with H₂), for each species of interest. In particular, we use CH₃OH rates from Pottage, Flower & Davis (2004), NH₃ rates from Danby et al. (1988), OCS rates from Green & Chapman (1978) and Schöier et al. (2005) and HC₃N rates from Green & Chapman (1978). The calculation is similar to that of Schöier et al. (2005), and calculates the strength of the emission line for a species and transition of interest, for a given density, temperature and column density.

To derive a column density for a given species, the integrated line intensity, $\int T_R^* dv$ in K.km/s, is found as a function of both density (n_{H_2}) and column density. The source is assumed to fill the beam. Initially we assume some temperature and the line width for each line of interest is taken from the observations in Table 2. The constant contour of the observed integrated line intensity can then be traced. This will usually give an upper or lower limit to the column density. With more than one line, it is often possible to simultaneously derive both a column density and density, for a given temperature.

Figure 7a shows a plot of the integrated intensity as a function of n_{H_2} and column density assuming a temperature of 26 K for the CH₃OH(4_{2,2} – 4_{1,3})E line from Table 2, with a FWHM of 4.8 km s⁻¹. The observed 11.8 K km s⁻¹ contour is plotted as a dashed line. As the density is increased and LTE approached, the intensity becomes constant with

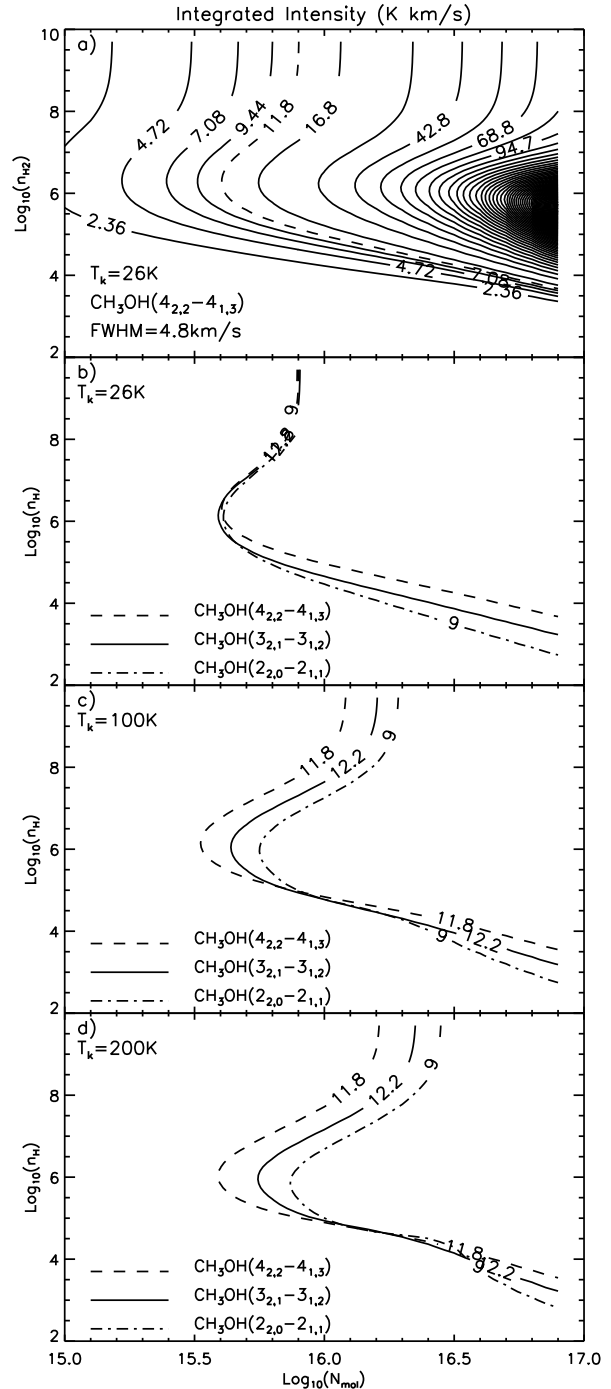


Figure 7. Contours of integrated intensity for rotational methanol transitions. (a) Integrated intensity of the CH₃OH 4_{2,2}–4_{1,3} transition calculated using a non-LTE theoretical model assuming a temperature of T=26 K. The constant contour which describes the observed intensity from Table 2 is plotted as the dashed line. (b) Comparison of the CH₃OH 4_{2,2}–4_{1,3} observed intensity from panel (a) with the CH₃OH 2_{2,0}–2_{1,1} and 3_{2,1}–3_{1,2} transitions calculated in a similar way for T=26 K using the values from Table 2. (c) and (d) are similar to panel (b), but for temperatures of 100 K and 200 K, respectively.

Table 3. Observations G305A from Steven Longmore (private communication 2007).

Observed line	Integrated Intensity (K km s ⁻¹)	Line Width (km s ⁻¹)
NH ₃ (1,1)	33.58	5.5
NH ₃ (2,2)	23.05	5.1
NH ₃ (4,4)	22.23	7.9

column density. Hill et al. (2005) report a density of the order $n_{\text{H}_2} \sim 1 - 2 \times 10^4 \text{ cm}^{-3}$, implying a column density of $\sim 4 \times 10^{16} \text{ cm}^{-2}$ from Figure 7a. However, the two other lines observed for CH₃OH can be used to further restrict the column density.

In Figure 7b, the corresponding constant contours of each observed integrated line intensity for all three CH₃OH lines are over-plotted. All three lines overlap and agree for $n_{\text{H}_2} > 10^6 \text{ cm}^{-3}$, yielding the LTE limit of the column density. Since the observations of Hill et al. (2005) suggest a lower density, it is likely that the gas is not in LTE. In Figures 7c and 7d, the same lines are over-plotted assuming temperatures of 100K and 200K. In each of these cases, there is agreement for densities and column densities in the ranges $1.8 \times 10^4 \text{ cm}^{-3} < n_{\text{H}_2} < 8 \times 10^4 \text{ cm}^{-3}$ and $7.9 \times 10^{15} \text{ cm}^{-2} < N < 2.0 \times 10^{16} \text{ cm}^{-2}$ respectively. Since all three lines agree for both temperatures, this method does not constrain the temperature. However, as previously mentioned, temperatures of 90 K or more are expected to evaporate CH₃OH off grain surfaces, and so we favour a temperature of at least 100 K.

High spectral and spatial resolution ammonia observations have been carried out (Steven Longmore, private communication 2007) for the (1,1), (2,2) and (4,4) lines. The details of the detection of these lines coincident with G305A are given in Table 3. A similar analysis to that of Figure 7 for the three NH₃ lines is shown in Figure 8. In Figure 8a, the temperature is 26 K, and clearly there is no agreement between the NH₃(4,4) line and the other two lines. However, if the temperature is increased, as in Figures 8b and 8c then there is closer agreement. The value derived from these plots for the column density is a little ambiguous since the (1,1) and (2,2) contours only converge as n_{H_2} decreases, so we only quote a lower limit of $N_{\text{NH}_3} > 10^{15} \text{ cm}^{-2}$. However, it is important to note that the observation of the NH₃(4,4) strongly suggests that there is a temperature in excess of 100 K.

We note that densities of $1.8 \times 10^4 - 8 \times 10^4 \text{ cm}^{-3}$ are unusually low for traditional hot core densities ($\sim 10^6 \text{ cm}^{-3}$). However, complex organic molecules are seen in extended emission in SgrB2 and in the central molecular zone (Requena-Torres et al. 2006). Requena-Torres et al. (2006) find that these molecules, including CH₃OH, can have low excitation temperatures (10-20 K) despite high kinetic temperatures (~ 100 K) and cold dust (< 20 K) because the density is low ($\sim 10^4 \text{ cm}^{-3}$). They argue that shocks remove mantle material and drive ‘hot core’ type chemistry. So low excitation temperatures may not necessarily reflect cold gas-phase chemistry.

We cannot do a complete analysis of OCS and HC₃N, with only single transitions for each. However we can give

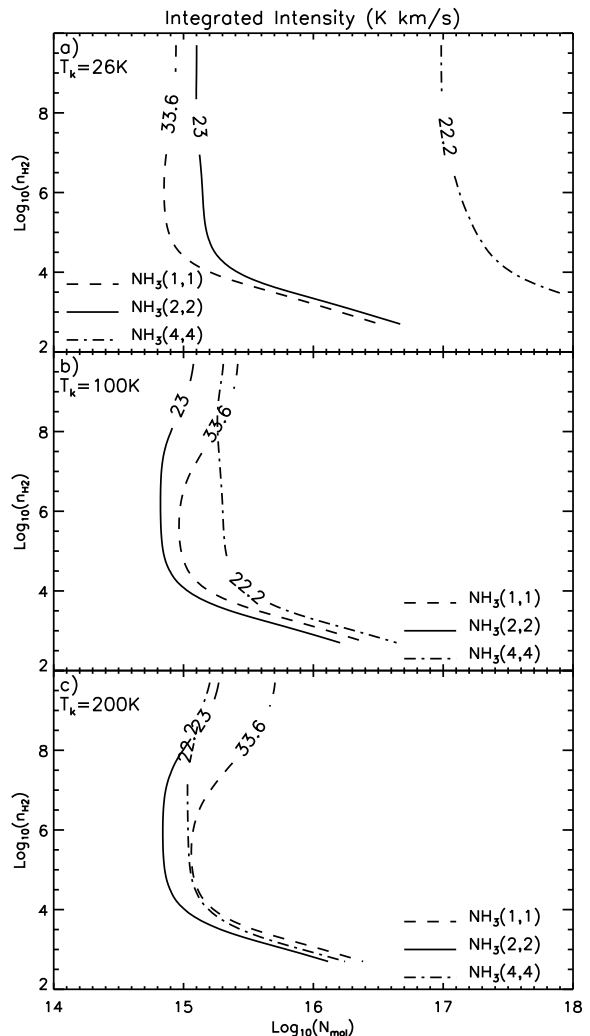


Figure 8. Contours of integrated intensity for rotational ammonia transitions. (a) Integrated intensities of the NH₃ rotation transitions (1,1), (2,2) and (4,4) calculated using a non-LTE theoretical model assuming a temperature of $T=26$ K. The chosen contours are taken from the observed intensities of Table 3. In panels (b) and (c) the same comparisons are made, assuming temperatures of 100 K and 200 K, respectively.

new values assuming densities in the range $1.8 \times 10^4 \text{ cm}^{-3} < n_{\text{H}_2} < 8 \times 10^4 \text{ cm}^{-3}$. Figure 9 shows the OCS(2-1) and HC₃N(2-1) lines plotted for 100K and 200K. For densities in the range $1.8 \times 10^4 \text{ cm}^{-3} < n_{\text{H}_2} < 8 \times 10^4 \text{ cm}^{-3}$, we can put limits on the column densities, which are given in Table 4 for 100K, along with the other non-LTE values for NH₃ and CH₃OH. We note that column densities derived here compare well to those derived in sections 4.2, 4.3 and 4.5, which assume LTE. This indicates that column densities derived under the assumption of LTE, at least in the case of G305A, may provide reasonable estimates of the true column density.

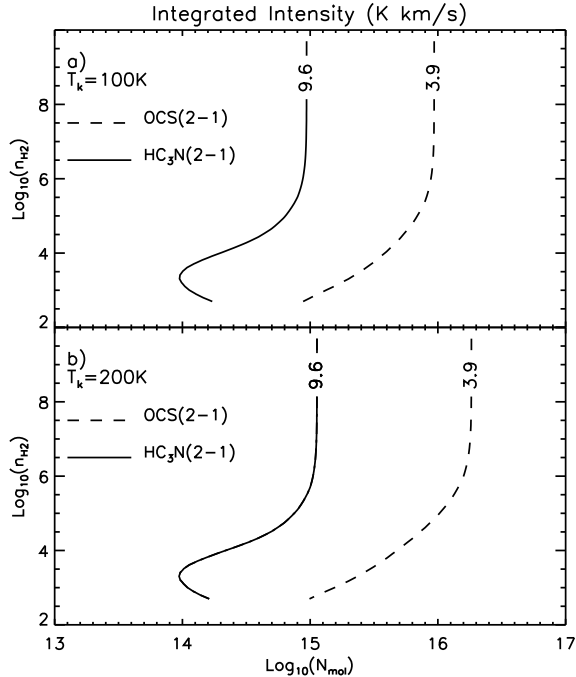


Figure 9. Contours of integrated intensity for rotational OCS and HC₃N transitions. (a) Integrated intensities of the OCS (2–1) and HC₃N rotation transitions calculated using a non-LTE theoretical model assuming a temperature of T=100 K. The chosen contours are taken from the observed intensities of Table 2. (b) The same transitions are presented as in panel (a), but with a temperature of 200 K.

Table 4. Column densities for G305A from §4.8, for $1.8 \times 10^4 \text{cm}^{-3} < n_{\text{H}_2} < 8 \times 10^4 \text{cm}^{-3}$.

Molecule	Column Density (cm^{-2})
CH ₃ OH	$7.9 \times 10^{15} \text{cm}^{-2} < N < 2.0 \times 10^{16} \text{cm}^{-2}$
NH ₃ *	$> 10^{15}$
OCS(100K)	$4.0 \times 10^{15} < N_{\text{OCS}} < 6.3 \times 10^{15}$
OCS(200K)	$5.6 \times 10^{15} < N_{\text{OCS}} < 9.5 \times 10^{15}$
HC ₃ N(100K)	$2.0 \times 10^{14} < N_{\text{HC}_3\text{N}} < 6.3 \times 10^{14}$
HC ₃ N(200K)	$2.8 \times 10^{14} < N_{\text{HC}_3\text{N}} < 6.3 \times 10^{14}$

* value derived from observations of Steven Longmore (private communication, 2007).

5 TIME-DEPENDENT CHEMISTRY

The analysis in section 4, in particular the detection of the NH₃ (4,4) line, strongly suggest that G305A has a hot component with a temperature of the order 100 – 200 K. We will therefore now model the chemistry of G305A, based on the assumption that it is a hot core. The time dependent chemistry of a spherical core, representative of G305A, will be calculated below and the observations will be discussed in light of these results. A molecule found inside a hot core may be present due the following three processes: if it is either formed by cold chemistry in the earlier core collapse phase then accreted onto a grain and re-released inside the hot core, formed by grain surface chemistry and released, or formed in the gas phase chemistry of the hot core. Although

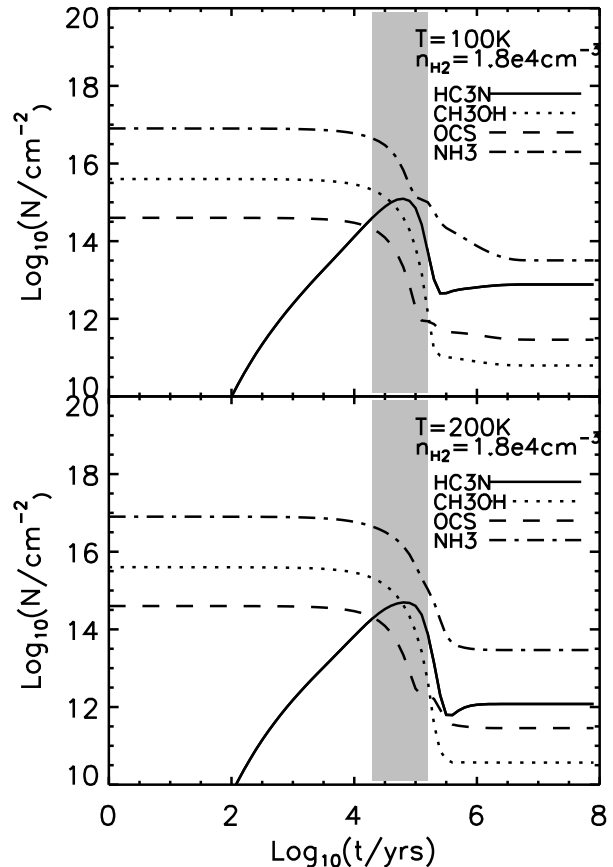


Figure 10. Time dependent column densities for the four species of interest, as calculated from a spherical hot core chemical model of G305A as described in §5. A constant density is assumed, $n_{\text{H}_2} = 1.8 \times 10^4 \text{cm}^{-3}$, with a temperature of 100 K (top panel) or 200 K (bottom panel). A comparison of a species column density constrains the age of the core. The grey shaded bar illustrates the age range of the core derived in comparing the observed column densities given in Table 4.

the mantle compositions are relatively simple e.g. CH₃OH and NH₃, the release of these into the gas phase are believed to be the drivers of the very complex chemistry observed in hot cores. The relative abundances of the mantle species, along with varying densities and temperatures can lead to chemical differences among cores.

We now attempt to model the gas phase chemistry of G305A. We assume the core is spherical with a density $n_{\text{H}_2} = 1.8 \times 10^4 \text{cm}^{-3}$ and $n_{\text{H}_2} = 8 \times 10^4 \text{cm}^{-3}$ based on the analysis in section 4.8, and a radius of 1.1 pc (Hill et al. 2005). The model is run twice with constant temperatures throughout of 100 K and 200 K. We use a model similar to Millar et al. (1997), which consists of 22 depth points, or shells, each with a specified density and temperature. Column densities are calculated by integrating along lines of sight, and to account for beam dilution, the column densities are weighted and summed over a gaussian beam (eg., Thompson, Macdonald & Millar 1999). The source is assumed to fill the beam. 211 species are chosen with 2575 reactions and rate coefficients, taken from the online UMIST database (Le Teuff et al. 2000).

The initial abundances are taken from Table 2 of Millar et al. (1997) which assumes that the gas is mostly

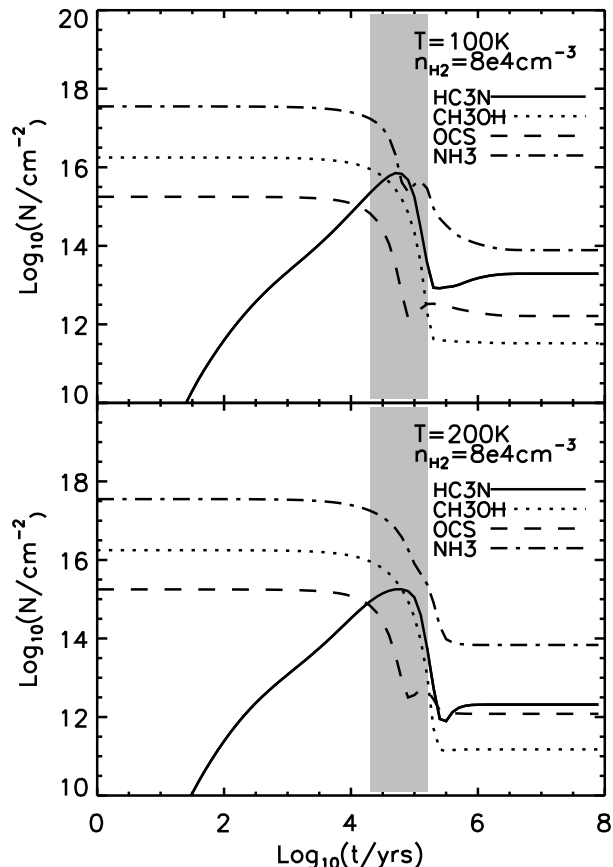


Figure 11. Column densities from the spherical core model, similar to Figure 10, but with the density increased to $n_{\text{H}_2} = 8 \times 10^4 \text{cm}^{-3}$.

molecular with some ionization by cosmic rays. Assuming spontaneous evaporation from grain surfaces, there are also the primary injected mantle molecules CH_3OH , NH_3 , C_2H_2 , C_2H_4 , C_2H_6 , CH_4 , H_2CO , CO_2 , O_2 , H_2O , H_2S . Ice absorption spectra towards massive young stellar objects suggest that OCS should also be included as a mantle species (Keane et al. 2001). We also find that an initial abundance of OCS is needed in the model to generate an OCS abundance that resembles the observations, the gas phase chemistry alone cannot produce the observed column density (see the discussion for Figures 10 and 11 below). The initial abundances are given in Table 5 which are based on the models of Millar et al. (1997) and Nomura and Millar (2004). The initial conditions are also chosen so that the total abundance of C, N and O do not exceed with the mean interstellar values; $\text{C}/\text{H} = 1.4 \times 10^{-4}$, $\text{O}/\text{H} = 3.19 \times 10^{-4}$ and $\text{N}/\text{H} = 7.5 \times 10^{-5}$ (Cardelli et al. 1996; Meyer et al. 1997, 1998). It should be noted that differences in the mantle chemistry and choice of initial abundances could drive a different gas phase chemistry, this will be considered in future papers, and is outside the scope of the current work.

The model results are presented in Figures 10 and 11 for $n_{\text{H}_2} = 1.8 \times 10^4 \text{cm}^{-3}$ and $n_{\text{H}_2} = 8 \times 10^4 \text{cm}^{-3}$, respectively. The column densities of the four species of interest are plotted as a function of time since the onset of the core heating. In each figure the chemical model has been run twice assuming temperatures of 100 K and 200 K. By comparing the

Table 5. The initial abundances, with respect to H nuclei, assumed in the chemical model

Species	Abundance	Species	Abundance
CH_3OH	5×10^{-7}	C_2H_2	5×10^{-7}
NH_3	1×10^{-5}	C_2H_4	5×10^{-9}
H_2S	1×10^{-6}	C_2H_6	5×10^{-9}
H_2O	1×10^{-5}	CH_4	2×10^{-7}
O_2	1×10^{-6}	CO_2	5.0×10^{-6}
H_2CO	4×10^{-8}	OCS	5.0×10^{-8}
CO	5×10^{-5}	N_2	2×10^{-7}
He^+	2.5×10^{-11}	H^+	1×10^{-10}
H_3^+	1×10^{-8}	Si^+	3.6×10^{-8}
Fe^+	2.4×10^{-8}		

column densities for each species in Table 4, derived from the observed emission lines in Table 2, the chemical model can be used to constrain both the temperature and age of the core. In the gas phase, the production of CH_3OH is very inefficient (eg. Woodall et al. (2007)); going via radiative association of CH_3^+ and H_2O at a low rate (Luca, Voulet & Gerlich 2002), while Geppart et al. (2006) have recently shown that the fraction of dissociative recombinations which produce methanol are of the order 3%. From the methanol column density limits quoted in Table 4, upper age limits are derived in Figure 11 for $n_{\text{H}_2} = 8 \times 10^4 \text{cm}^{-3}$; 3.1×10^4 years for 100 K and 2×10^4 years from 200 K. The lower density $n_{\text{H}_2} = 1.8 \times 10^4 \text{cm}^{-3}$ cases of Figure 10 do little to constrain the age since $N_{\text{CH}_3\text{OH}} < 7.9 \times 10^{15} \text{cm}^{-2}$. From the NH_3 observations, both Figures 10 and 11 give upper age limits of 1.6×10^5 years.

The column density of HC_3N indicates either, a minimum age of $\sim 10^4$ years, or an age of 10^5 years. We favor the later time based on the NH_3 comparisons discussed above. As noted by Millar et al. (1997), HC_3N is usually regarded as a cold cloud tracer, however it is formed in a hot gas through reactions of N and C_3H_2 and C_2H_2 with CN, where C_2H_2 is evaporated from grain mantles. This suggests that HC_3N should be a useful species to trace the conditions and ages of hot cores. The highly variable HC_3N abundance with time, in Figures 10 and 11, further supports the use of HC_3N as a ‘chemical clock’ species.

The OCS column densities quoted in Table 4 are $> 4 \times 10^{15} \text{cm}^{-3}$, which is higher than the maximum OCS column density for all cases. The observed OCS abundance can be reproduced in the model if the initial abundance of OCS was increased. For simplicity, we assumed the OCS abundance from Nomura and Millar (2004) based on their model of G34.3+0.15, and so it is highly possible that the initial OCS abundance was greater for G305A. We will examine the effects of changes in the model for varying initial conditions in future papers. It is important to note that if no initial abundance of OCS is assumed in the model, then the gas phase chemistry only produces a OCS column density of the order $4 \times 10^{13} \text{cm}^{-2}$ (plots not shown here), which strongly suggests that the origin of the OCS is the evaporated ice mantles. Moreover, OCS has been detected in ice-absorption features of massive protostars (Keane et al. 2001).

It is important to note that the column densities of NH_3 and HC_3N give similar core ages, $\sim 10^5$ years, for each

of the 4 cases plotted in Figures 10 and 11. However, the determination of the temperature and density is still a little ambiguous. There is better agreement for NH_3 and HC_3N times for the denser hotter case. Moreover, the NH_3 observations (Steven Longmore, private communication 2007) discussed in §4.8 (in particular Figure 8) suggest higher temperatures of the order 200 K. We therefore favor the high density $8 \times 10^4 \text{cm}^{-3}$ and 200 K case, suggesting a core age in the range $2 \times 10^4 < t_{\text{core}} < 1.5 \times 10^5$ years.

6 CONCLUSIONS

We have observed the massive star forming region G305.2+0.2 at 1.2 cm. We detected emission in methanol, cyanoacetylene, ammonia, carbonyl sulfide and water, as well as the radio recombination line H91 β . All molecular transitions are detected towards G305A, which confirms the hot core nature of this source. Three lines of methanol are found in emission at the position of G305A, and together with a fourth transition which was not detected, we have constructed a rotational diagram where we derive a rotational temperature of 26 K and a column density of $9.6 \times 10^{15} \text{cm}^{-2}$ for methanol. However, because methanol requires temperatures in excess of 90 K to evaporate from dust grains, we find the temperature unrealistic and attribute this to the incorrect assumption of LTE. With a non-LTE analysis of G305A, we derive a model which is consistent with a density of $8 \times 10^4 \text{cm}^{-3}$, and a temperature of the order 200 K. A gas phase time dependent chemical model further constrains the age of the core to $2 \times 10^4 < t_{\text{core}} < 1.5 \times 10^5$ years.

Extended emission to the SE of G305A is seen in three methanol transitions. It has a narrow line width and an unusually high rotational temperature (78 K). We interpret this as evidence that the emission may be a weak maser.

Strong methanol maser emission is found 3'' to the east of G305B. Since the methanol transition at 24.933 GHz is a Class I maser, G305B appears to be a unique object worthy of further investigation as it shows both Class I and II methanol maser emission within a small region. No other detections were made at the position of G305B. Since it is also known to be a luminous source, the lack of molecular emission suggests G305B is an older source that has already had time to clear out its surrounding molecular material.

Radio continuum emission at 18.496 GHz is detected towards two HII regions (G305HII and G305HII(SE)). G305HII shows a cometary morphology and is probably powered by a star in the range O8 to B0, whereas G305HII(SE) shows a shell morphology and is probably powered by a star in the range O9.5 to B0.

No radio continuum emission was detected towards either G305A or G305B. For the case of G305A, this may be because the source is too young to have produced an observable HII region. However, it is not clear why the older, and infrared-luminous, source G305B does not show any radio continuum emission.

ACKNOWLEDGMENTS

We would like to thank the anonymous referee who has helped improve the quality of this work. We would like to thank Andrej Sobolev for helpful discussions. We would also like to acknowledge the work of Steven Longmore who helped with discussions and data of ammonia. The Australia Telescope is funded by the Commonwealth of Australia for operation as a National Facility managed by CSIRO. This research was supported under the Australian Research Council's Discovery funding scheme (project number DP051893). Astrophysics at QUB is supported by a grant from PPARC.

REFERENCES

- André, P., Ward-Thompson, D. & Barsony, M. 1993, ApJ, 406, 122
- Bergin, E. A., Ungerechts, H., Goldsmith, P. F., Snell, R. L., Irvine, W. M. & Schloerb, F. P. 1997, ApJ, 482, 267
- Cardelli, J.A., Meyer, D.M., Jura, M., Savage B.D. 1996, ApJ, 467, 334
- Charnley, S. B. 1997, ApJ, 481, 396
- Charnley S.B., Tielens A.G.G.M., Millar T.J. 1992, ApJ, 399,L71
- Cragg, D. M., Sobolev, A. M. & Godfrey, P. D. 2002, MNRAS, 331, 521
- Danby, G., Flower, D. R., Valiron, P., Schilke, P. & Walmesley, C.M. 1988, MNRAS, 235, 229
- De Buizer, J. M. 2003, MNRAS, 341, 277
- Dickman, R. L. 1978, ApJS, 37, 407
- Forveille, T., Guilloteau, S., & Lucas, R. 1989, CLASS Manual (Grenoble: IRAM)
- Fukuzawa, K. & Osamura, Y., 1997, ApJ, 489, 113
- Geppert, W. D., Hamberg, M., Thomas, R. D., Osterdahl, F., Hellberg, F., Zhaunerchyk, V., Ehlerding, A., Millar, T.J., Roberts, H., Semaniak, J., af Ugglas, M., Kallberg, A., Simonsson, A., Kaminska, M. & Larsson, M., 2006, Faraday Discuss. 133, 177
- Green, S. & Chapman, S. 1978, ApJS, 37, 169
- Hartquist, T. W., Dalgarno, A. & Oppenheimer, M. 1980, ApJ, 236, 182
- Hatchell, J., Thompson, M. A., Millar, T. J. & MacDonald, G. H., 1998, MNRAS, 338, 713
- Hill, T., Burton, M. G., Minier, V., Thompson, M. A., Walsh, A. J., Hunt-Cunningham, M. & Garay, G. 2005, MNRAS, 363, 405
- Keane, J. V., Tielens, A. G. G. M., Boogert, A. C. A., Schutte, W. A., Whittet, D. C. B. 2001, A&A, 376, 254
- Keto, E. 2003, ApJ, 599, 1196
- Kurtz, S., Churchwell, E. & Wood, D. O. S. 1994, ApJS, 91, 659
- Le Teuff Y. H., Millar T. J. & Marwick A. J. 2000, A&AS, 157, 146
- Linke, R. A., Frerking, M. A. & Thaddeus, P. 1979, ApJ, 234, L139
- Luca, A., Voulet, D. & Gerlich, D., 2002, WDSO2 Proceedings of Contributed papers, Part II, 294
- Meyer, D. M., Cardelli, J. A. & Sofia, U. J. 1997, ApJ, 490, L103
- Meyer, D. M., Jura, M. & Cardelli, J. A. 1998, ApJ, 493, 222

- Millar T. J., Macdonald G. H., & Gibb A. G. 1997, *A&A*, 325, 1163
- Minier, V., Ellingsen, S. P., Norris, R. P. & Booth, R. S. 2003, *A&A*, 403, 1095
- Moscadelli, L., Cesaroni, R. & Rioja, M. J., 2005, *A&A*, 438, 889
- Müller, H. S. P., Menten, K. M. & Mäder, H., 2004, *A&A*, 428, 1019
- Nomura, H. & Millar, T. J. 2004, *A&A*, 414, 409
- Norris, R. P., Whiteoak, J. B., Caswell, J. L., Wieringa, M. H. & Gough, R. G., 1993, *ApJ*, 412, 222
- Panagia, N. 1973, *AJ*, 78, 929
- Phillips, C. J., Norris, R. P., Ellingsen, S. P. & McCulloch, P. M. 1998a, *MNRAS*, 300, 1131
- Pirogov, L., Zinchenko, I., Caselli, P., Johansson, L. E. B. & Myers, P. C. 2003, *A&A*, 405, 639
- Pottage, J. T., Flower, D. R. & Davis, S. L. 2004, *MNRAS*, 352, 39
- Requena-Torres, M. A., Martín-Pintado, J., Rodríguez-Franco, A., Martín, S., Rodríguez-Fernández, N. J. & de Vicente, P. 2006, *A&A*, 455, 791
- Schöier, F. L., van der Tak, F. F. S., van Dishoeck E. F. & Black, J. H. 2005, *A&A* 432, 369
- Tafalla, M., Myers, P. C., Caselli, P., Walmsley, C. M. & Comito, C. 2002, *ApJ*, 569, 815
- Tielens A. G. G. M. & Allamandola L. J. 1987, in *Physical Processes in Interstellar Clouds*, ed. G.E. Morfill and M Scholer, Dordrecht: Kluwer, 333
- Thompson M. A., Macdonald G. H., Millar T. J. 1999, *A&A*, 342, 809
- Ungerechts, H., Bergin, E. A., Goldsmith, P. F., Irvine, W. M., Schloerb, F. P., & Snell, R. L. 1997, *ApJ*, 482, 245
- Voronkov, M. A., Sobolev, A. M., Ellingsen, S. P. & Ostrovskii, A. B., 2005, *MNRAS*, 362, 995
- Walsh, A. J., Burton, M. G., Hyland, A. R., Robinson, G., 1998, *MNRAS*, 301, 640
- Walsh, A. J., Burton, M. G., Hyland, A. R. & Robinson, G. 1999, *MNRAS*, 309, 905
- Walsh, A. J., Bertoldi, F., Burton, M. G. & Nikola, T. 2001, *MNRAS*, 326, 36
- Walsh, A. J. & Burton, M. G. 2006, *MNRAS*, 365, 321
- Woodall, J., Agundez, M., Markwick-Kemper, A.J. & Millar, T.J., 2007, *A&A*, in press